

Polycatenated Architected Materials

Wenjie Zhou,¹ Sujeeka Nadarajah,¹ Liuchi Li,² Anna Guell Izard,³ Aashutosh K. Prachet,¹ Payal Patel,¹ Hujie Yan,¹ Xiaoxing Xia*,³ and Chiara Daraio*¹*

Affiliations

¹Division of Engineering and Applied Science, California Institute of Technology, Pasadena, CA, USA

²Hopkins Extreme Materials Institute, Johns Hopkins University, Baltimore, MD, USA

³Lawrence Livermore National Laboratory, Livermore, CA, USA

*Correspondence to: zhouw@caltech.edu, xia7@llnl.gov, daraio@caltech.edu

Abstract:

Architected materials derive their properties from the geometric arrangement of their internal structural elements, rather than solely from their chemical composition. They can display remarkable behaviors such as high strength while being lightweight^{1,2}, negative Poisson's ratios^{3,4}, and shear-normal coupling^{5,6}. However, architected materials so far have either exhibited solid-like^{1,2} or fluid-like behavior^{7,8}, but not both. Here, we introduce a class of materials that consist of linked particles assembled in three-dimensional domains, forming polycatenated architected materials (PAMs). We propose a general framework for PAMs that translates arbitrary crystalline networks into particles' concatenations and design particles' geometry. The resulting materials are cohesive, yet the individual particles retain some kinematic freedom. In response to small external loads, PAMs behave like non-Newtonian fluids, showing both shear-thinning and shear-thickening responses. At larger strains, PAMs behave like solids, showing a nonlinear stress-strain relation, like lattices and foams. These responses are regulated by a jamming transition determined by the

particles' arrangement and the direction of loading. PAMs are scalable, showing comparable mechanical responses at both millimeter- and micrometer-scales. However, micro-PAMs can change shape in response to electrostatic charges. PAM's properties are relevant for developing stimuli-responsive materials, energy-absorbing systems and morphing architectures.

Main Text:

Introduction

Most architected materials have been designed using rigidly connected truss^{-1,9}, plate^{-10,11}, or shell-based lattices^{12,13} that derive effective bulk properties from periodically repeating unit cells^{14,15}, or disordered architectures^{16,17}. Depending on the geometry of their interior structure, they exhibit unusual or extreme mechanical properties^{1,2}, such as large reconfigurability¹⁸⁻²², multi-stable responses^{23,24} and nonlinear elastic deformations^{25,26}. In some realizations, architected materials behave like fluids, like pentamode materials, which present a near-zero shear response^{7,8}. Granular crystals and topologically interlocked panels are a type of architected materials that consist of regular arrays of closely packed elements that interact elastically^{27,28}. They also present rich mechanical properties, such as geometrical hardening²⁹ and nonlinear wave propagation²⁸, which emerge from the geometry of the individual particles, their topological arrangement and the particles' chemical composition. However, in the absence of boundary confinement, granular crystals are not cohesive, because the particles are not held together by binders, and they offer no resistance in tension.

An emergent family of architected materials are topologically interlocked fabrics, consisting of layers of polycatenated particles, like chainmails, which have been shown to support tunable

stiffness and controllable shape morphing^{30,31}. The concept of polycatenation, rooted in polymer and supramolecular chemistry^{32–34}, refers to the intricate interlinking of molecular structures, typically seen in polycatenated metal-organic frameworks (MOFs) and covalent organic frameworks (COFs)^{32,33,35,36}. The polycatenation of knots and weave-like patterns have been explored through the lens of geometry, introducing a unique facet of reticular chemistry^{32–34}.

Here, we integrate the principle of polycatenation into three-dimensional (3D) architected materials that we fabricate at the macro- and micro-scales, to create cohesive arrangements of discrete particles with controllable kinematic degrees of freedom (DOFs). We propose a design strategy to translate continuous graph topologies, such as crystalline lattices³⁷, into their polycatenated counterparts and demonstrate the realization of 3D polycatenated architected materials (PAMs) from selected building blocks. We show how local variations in the particles' geometry affects the internal DOFs, which, in turn, control the global deformability and effective response of the bulk. Because of the discrete nature of the particle-particle interactions in PAMs, their global mechanical behavior transitions from fluid-like to solid-like, as a function of the applied loading and their response can be preconditioned by repeated loading cycles. We show that PAMs are lightweight and, as opposed to other lattice-based architected materials, they express isotropic responses to different loading conditions. PAMs are resilient to cyclic loading and have tunable energy absorption, with scalable responses that persist at both the macro- and micro-scales.

Design approach for PAMs

Conversion of continuous graph topologies into PAMs. Traditional lattice structures can be mapped into continuous topological networks that consist of nodes and connections (Fig. 1a). Starting from arbitrary networks, we create periodically entangled toroidal, polygonal, or polyhedral caged particles (hereinafter referred to as 'particles') that can be tessellated into PAMs

at different scales. The process begins by identifying node symmetries in the continuous networks and aligning them with particles that possess these symmetries. These particles interlink with adjacent ones, replicating the original network connections (Figs. 1a-c). Thanks to the enormous database of crystallographic symmetries, topological networks from databases like RCSR³⁷ can be transformed into polycatenated analogs (Extended Data Fig. 1). A single node can be represented using particles with various particle shapes, such as polyhedral wireframes, polygon clusters, or torus clusters (Fig. 1d). Depending on the nature of the constituent units, the topologies of resulting polycatenated architectures exhibit substantial variations (Fig. 1e).

Generating 3D PAMs from prescribed particle geometries. A given particle shape can exhibit multiple symmetry axes (Fig. 1f), leading to several potential catenation environments (Figs. 1g-i). By utilizing these catenations singularly or in combination, we can create a variety of PAMs (Figs. 1j-m), each with its own global topology. We employ a tripartite naming scheme, **X-n-abc**, for easy identification: ‘X’ for the network topology, ‘n’ for the symmetry of local catenation, and ‘abc’ for the particle shape, either in full or as an acronym. As an example, the label **D-3-tet** (Fig. 1c) denotes a polycatenated diamond network (**D**) constituted from tetrahedral wireframes (**tet**) that interlock corner-to-corner by aligning their 3-fold axes (**3**).

By changing the particles’ shapes within similar symmetries (like from octahedra to cuboctahedra) within a given topology (Extended Data Fig. 2, Supplementary Video 6), we can alter the locking mechanisms (e.g., transitioning from a corner-to-corner linking, as in a J-2-oct to an edge-to-edge interlocking in the J-2-CO), thus varying the DOFs between particles (Extended Data Fig. 2). Reducing the particles’ thickness, thereby decreasing the volume fraction, typically increases the kinematic DOFs between units within the same global topology and the resulting mechanical response of the PAMs.

PAM fabrication

We fabricated eight representative PAMs, four composed of 2D particles (Figs. 2a-d) and four composed of 3D particles (Figs. 2i-l), using a brittle acrylic polymer using additive manufacturing (see Methods). Each sample was designed to be a cube with side ca. 50 mm (Figs. 2e-h, 2m-p). To maintain 0.1 mm particle-particle separation, wax was used as support materials and later dissolved. Upon removal of the support materials, the PAMs relaxed under gravity and the originally ordered and periodic microstructure became irregular (Figs. 2e-h, 2m-p). Designed and relaxed dimensions are summarized in the Extended Data Table 1.

PAMs are characterized by their catenation number (CN), defined as the number of neighboring particles that are catenated with the center one, represented using ball-and-stick models³⁸ (Figs. 2a-d, 2i-l). The same CN can represent multiple local particle arrangements. For example, CN = 4 in a planar arrangement maps to a network with a **nbo** topology, while CN = 4 in a tetrahedral (T_d) arrangement maps to a network with a **dia** topology³⁷.

J-2-ring (Fig. 2a) and J-2-sqr (Fig. 2b) were designed to compare the influence of particle geometry while keeping the PAM topology constant. T-2-ring (Fig. 2c) and T-2-hex (Fig. 2d) served as another pair of comparison. J-2-oct (Fig. 2i) and S-4-oct (Fig. 2j) were designed to compare the influence of PAM topology while keeping the particle geometry constant. D-3-tet (Fig. 2k) and C-2-TT (Fig. 2l) were designed because they are two results of geometric transformations from T-2 topology – D-3-tet emerge when every two tetrahedral clusters catenated through 3-fold axes are transformed into a pair of tetrahedra; while C-2-TT emerge when every two tetrahedral clusters catenated through 2-fold axes are transformed into a pair of truncated tetrahedra (Extended Data Fig. 2). Notably, J-2-sqr has two stable configurations (Supplementary Video 7): an expanded, stiff configuration (L); and a collapsed, flexible configuration (S). Configuration L can transition

into S via an auxetic mechanism like the ‘rotating squares behavior’³⁹ (Supplementary Video 8), which can be trained by cyclic application of external loading. To minimize structural randomness, we standardized the maximum permissible particle thicknesses to maintain clearances as 0.1 mm in all designs except for J-2-oct and S-4-oct.

Mechanical characterization of PAMs

To characterize the mechanical response of PAMs, we conducted compression, shear, and rheology tests under different loading conditions. The mechanical response of PAMs emerges from a complex interplay of interactions across scales, ranging from (i) μm -scale inter-particle contacts, (ii) mm-scale particle deformation (e.g., bending, buckling and fracture), (iii) mesoscale layer-by-layer collapse, and (iv) cm-scale global deformations. Initially, all loadings induce the rearrangement of particles within the available kinematic DOFs and the redistribution of stresses within the volume, without damage to the particles. However, the particles’ rearrangement leads to a bulk deformation of PAMs, which persists even after the removal of the external loads. As the particles reach a jammed state, further spatial reconfiguration becomes untenable. Beyond jamming, continued compressive forces result in particles’ deformation, damage and fracture.

Under uniaxial compression (Figs. 3a-g, Supplementary Video 3, Extended Data Fig. 4), all samples exhibit a nonlinear stress-strain behavior with significant loading/unloading hysteresis (energy absorption). This hysteric stress-strain relationship is likely influenced by three distinct mechanisms: (i) the rearrangement of catenated particles, (ii) the presence of friction, and (iii) at larger strains, particle deformation and damage.

Repeated loading and unloading cause PAMs to develop a permanent residual strain. Under cyclic compression at lower strains, PAMs show a reduced peak stress and a hysteretic response

with a progressively smaller area, leading to less energy being dissipated in each cycle (Extended Data Fig. 4). Most of this reduction happens within the first few cycles, after which the PAMs stabilize into a steady-state response. This initial drop in energy dissipation, known as preconditioning, is a common characteristic of many rubbery⁴⁰ and biological⁴¹ materials. Under cyclic compression with progressively increasing strain (from 10% to 50%), the material continues to follow the primary loading path until extensive damage occurs, as long as the strain in each cycle exceeds the maximum strain of the previous cycle (Fig. 3a-g). These observations mirror the Mullins effect seen in certain rubbers⁴⁴.

In granular systems, particles' shape significantly affects macroscopic mechanical properties^{30,42}, this can also be observed in PAMs. T-2-ring and T-2-hex exhibit comparatively lower stiffness and can withstand maximum strain without damage to their constituent units (Figs. 3a,b), unlike PAMs composed of polyhedral particles (Figs. 3c,f,g). This discrepancy can be attributed to the fact that jamming in polyhedron-based PAMs occurred at lower strain values than in 2D polygons or rings (Figs. 3a-g). Additionally, the larger number of kinematic DOFs and the coupled deformation modes of rings and hexagonal particles resulted in lower overall PAM's stiffness. This phenomenon is reminiscent of powders, where sphere-like particles (analogous to PAMs composed of polyhedral particles) are found to exhibit higher compressive strength and elastic modulus, as compared to flake-like particles (analogous to T-2-ring and T-2-hex)⁴³. PAMs with fewer kinematic DOFs, like J-2-ring, J-2-sqr, in addition to structures composed of polyhedral particles, displayed higher stiffness (Figs. 3d,e,h). Therefore, PAMs can be designed to present higher stiffness by (i) increasing the edge numbers of particles, or (ii) disrupting kinematic DOFs among particles.

Unlike other architected materials, PAMs exhibit a notable ability to adjust their interparticle arrangements in response to external loads, a characteristic also found in granular systems. This particles' rearrangement leads to two mechanical regimes, which appear under all deformation modes: (i) a fluid-like response, with a vanishing shear modulus, linked to relative particles' motion; and (ii) a solid-like response, characterized by particles' deformation, beyond the jamming transition. To describe the fluid-like mechanical response, we conducted shear and rheology tests on J-2-ring and T-2-ring samples (Figs. 4a,b). These PAMs were selected because they are composed of toroidal particles, which have greater kinematic DOFs. To control testing conditions, we fabricated samples that incorporated top and bottom gripping plates (Figs. 4a,b; Extended Data Fig. 3).

Under shear loads, both J-2-ring and T-2-ring samples demonstrated a plateau region with force values close to zero, indicative of a fluid-like behavior (Figs. 4c,f, Supplementary Video 3). Beyond a critical strain, such plateau then transitioned to a quasi-linear elastic region, typical of solid-like behavior. This transition can be correlated to the reduced DOFs between rings, which jam under external tensile, compressive or shear loads. The fluid-like and solid-like regimes can be programmed by designing the catenation topologies and particle geometries.

To further understand this fluid-solid duality, we characterized the rheological properties of cylindrical shaped PAM samples (Fig. 4b, Supplementary Video 4). In oscillatory amplitude sweep experiments (Figs. 4d,g), the J-2-ring and T-2-ring samples initially displayed a decrease in storage modulus (G'), loss modulus (G''), and complex viscosity (η^*) with increasing torsional strain. Upon reaching the critical jamming strain observed in simple shear tests, all three parameters begin to increase. This behavior parallels observations in certain shear thickening fluids. However, shear thickening fluids initially undergo only a minimal shear thinning phase that results in a small

reduction of viscosity⁴⁴. In contrast, PAMs show a much more significant reduction in viscosity, which decreases by several orders of magnitude (Figs. 4d,g).

In the frequency sweep experiments (Figs. 4e,h), both J-2-ring and T-2-ring samples exhibited an unusual inflection in viscosity at high angular frequency. When subjected to torsional strains below their respective jamming transition thresholds, a notable transition from shear-thinning to shear-thickening was observed with increasing oscillation angular frequency. This transition is likely due to the inertia effects of particles under high-frequency oscillation conditions.

To understand this unusual frequency-dependent thinning-to-thickening transition, we modeled the response of PAMs using the level-set discrete element method (LS-DEM)^{45,46}. We focus on modeling the rheological experiments, and the inflection of η^* with increasing angular frequency. Since the mechanical deformation of each particle is minimal compared to the translation observed in their rigid body motion (e.g., rearrangement) in the experiments, we model the rings as rigid particles. LS-DEM can model the contact dynamics among granular particles of arbitrary shapes, and it has been applied to model systems made of 3D-printed particles^{30,47}. Here, we use LS-DEM to model sweep experiments for both J-2-ring and T-2-ring samples. We construct digital twins, replicating the ring's shape, density, size, spatial arrangement, as well as the total number of rings in each respective sample.

All simulations qualitatively capture the inflection of η^* observed in experiments (compare Figs. 4i,k with Figs. 4e,h). Our simulations also agree with experiments in that the value of η^* at the inflection point is smaller for the J-2-ring sample compared to the that for the T-2-sample. However, the simulations overestimate the angular frequency at which the inflection of η^* happens. This mismatch could be due to imprecisions in the experimental particle geometry, contacts' imperfections and the presence of friction, which are not included in our models. These

discrepancies can also lead to considerable differences in the initial sample's packing structure in the relaxed configuration in experiments and simulations, which can shift the angular frequency at which the inflection of η^* happens. Nevertheless, our simulations provide particle-scale details that allow us to better understand the mechanisms underpinning this thinning-to-thickening transition. More specifically, from the point view of the rheophysics of dense granular materials⁴⁸⁻⁵⁰, η^* takes contribution from two components: a “contact” component (which corresponds to percolating force chains in the statics of granular media, used often in the soil mechanics community), and a “fluctuation” component (which corresponds to the degree of turbulency of granular flow, used often in the fluid mechanics community).

In our experiments, as the excitation frequency increases, it is expected that both samples experience a transition from a contact-dominant (or “quasi-static”) regime to a fluctuation-dominant (or “inertia”) regime. As such, the initial decrease of η^* can be understood as the decrease of contact (due to stronger centrifugal effects) in the contact-dominant regime, while the later increase of η^* can be understood as the increased degree of “turbulency” (due to a faster external excitations) in the fluctuation-dominant regime. This concept is confirmed by looking at Fig. 4j, which shows, for the simulation of the J-2 ring sample, the variation of the average contact number per particle, and of the normalized average particle velocity fluctuation (computed as the square root of *granular temperature*⁴⁸, see Methods for our calculation procedure), as functions of the angular frequency. As the angular frequency increases, the average contact number per particle decreases while the particle velocity fluctuation increases. In particular, the latter shows a much rapid increase rate once crossing the inflection point of η^* , which suggests the transition from the contact-dominant regime to the fluctuation-dominant regime. A similar observation can be made for the T-2 ring sample, by looking at Fig. 4l and comparing it to Fig. 4j.

Programmable critical jamming strains

We study the role of particle geometry and particle's linking topology in the jamming transition in PAMs. The local catenation topologies in PAMs play a pivotal role in defining their mesoscale (e.g., cell-to-cell, layer-by-layer) DOFs, which in turn dictates the critical strain for jamming (ϵ_c^* : critical compressive jamming strain; γ_s^* : critical shear jamming strain). For instance, J-2-ring PAMs show a significantly higher γ_s^* as compared to T-2-ring PAMs, whereas T-2-ring exhibits a higher ϵ_c^* relative to J-2-ring. In J-2-ring PAMs, shear loading induces a coordinated rearrangement of particles, thereby amplifying γ_s^* (Fig. 5a). During this process, rings oriented parallel to the shearing direction maintain their orientations, while those perpendicular to the shearing direction rotate in a coordinated manner, facilitating a greater γ_s^* . However, under compression or tension, the rings' inability to adjust their positions – restricted by limited DOFs from neighboring particles – results in a reduced ϵ_c^* . In contrast, T-2-ring PAMs rely on a 'scissor' mechanism (Fig. 5c): Upon compressive loading, all rings adjust their orientations coordinatively, which allows for a larger ϵ_c^* .

In addition to the choice of catenation topology, the thickness, d , of the torus significantly influences the jamming transition in PAMs (Fig. 5d). A decrease in d generally correlates with an increased DOF in PAMs. To elucidate this relationship, we fabricated a series of J-2-ring and T-2-ring PAMs with constant ring diameters (D) but varied d . We measured the critical jamming strain under both shear (γ_s^*) and compressive (ϵ_c^*) loading conditions as a function of thickness d (Fig. 5b). Regardless of the catenation topology, reductions in d are associated with increases in both γ_s^* and ϵ_c^* . Furthermore, we observed that catenation topology significantly impacts the predominant deformation modes. For instance, the γ_s^* for J-2-ring PAM (Fig. 5d), which exhibit the largest d/D

ratio and therefore the lowest DOF, is higher compared to T-2-ring PAMs (Fig. 5o), which have a much lower d/D ratio.

Length-scale dependence and electrostatic reconfiguration of μ -PAMs

The deformability of PAMs is primarily influenced by their particle geometries, which can be scaled across several particles' dimensions. This suggests that the mechanical responses of PAMs should remain consistent across scales (i.e., macroscopic to microscopic). To validate this hypothesis, we fabricate PAMs using multiphoton lithography and oxygen plasma etching (see Methods). Upon completion of the fabrication and activation process—where plasma etching removes thin support materials required during fabrication – the μ -PAMs demonstrated a gravitational relaxation analogous to that observed in their macroscopic counterparts (Extended Data Fig. 10). We designed a series of C-2-TT PAMs (as in Fig. 3c) varying their volume fractions, by changing the beam thicknesses of the particles. Following an increasing order of beam thickness, we label the PAMs as I, II, and III (Extended Data Fig. 6). The same PAMs were fabricated at both macroscale ($\Omega_I, \Omega_II, \Omega_III$) and microscale (μ_I, μ_II, μ_III), scaling them by a factor of 60 in all dimensions (i.e., sample side lengths: 24 mm and 400 μ m). Due to the differences in fabrication methods, we used slightly different acrylic polymers (Material properties in Methods) for the macro- and micro-scale samples. Nevertheless, we found qualitative agreement between the mechanical responses of PAMs across scales (Figs. 6a-c). The energy absorption capacities (U) of all C-2-TT PAMs were calculated by integrating the areas under the stress-strain curves. Our experiments reveal that scale factors (U_{μ}/U_{Ω}) among all I, II, III designs to be near constant of 12.76 ± 0.53 (Fig. 6a). To test if μ -PAMs also possess fluid-like properties, we tessellated J-2-ring μ -PAM voxels to form various geometries: a side-anchored cube (Fig. 6d), a point-anchored cube (Fig. 6e), a bottom-anchored numeral '1' (Fig. 6f), and a bottom-anchored letter 'T' (Fig. 6g).

One defining difference between micro-scale and macro-scale PAMs is their dramatically different surface-to-volume ratio ($\sim 3,600$ times larger in the μ -PAM samples). Such discrepancy can be exploited to observe the role of surface forces in the global deformation of PAMs. To test this hypothesis, we electroplated each μ -PAM sample with a thin layer of copper, approximately 300 nm in thickness, to provide electrical conductivity. We then positioned the samples atop a Van de Graaff generator with direct electrical contact (Extended Data Fig. 10). As electrostatic charge accumulated, the individual rings within the μ -PAMs began to repel each other, due to increased electrostatic repulsion. This electrostatic interaction prompted the μ -PAMs to both expand outward in all directions due to inter-ring repulsion and elongate upwards due to repulsion between the μ -PAMs and the substrate, transforming each initially relaxed structure into a structurally deployed state (Figs. 6d-g, Supplementary Video 6). The transition between the natural, compact state and the electrified, deployed state was fast (< 1 s, Supplementary Video 9) and completely reversible. This suggests that μ -PAMs driven by electrostatic forces can be engineered as responsive elements in remotely actuated materials, for micro-scale devices and smart material systems.

Discussions

Our work introduces PAMs as a novel class of architected materials, distinguished by their ability to exhibit both fluid-like and solid-like behaviors regulated by a jamming transition, which we demonstrate both at the macro- and micro-scales. By mapping discrete, topologically interlocked particles onto 3D crystalline networks, PAMs achieve programmable mechanical responses that can be precisely controlled by the particles' geometry and arrangement. The solid-fluid duality of PAMs opens new frontiers in the design of architected materials. Their nonlinear elastic response in the jammed state, coupled with non-Newtonian shear-thinning and shear-thickening behaviors in the unjammed state, provides a versatile mechanical platform for

applications requiring adaptive stiffness and energy dissipation. This is particularly relevant for stimuli-responsive materials, soft robotics, and morphing architectures. By leveraging the principles of polycatenation and topology, this work lays the foundation for creating architected materials with unprecedented control over mechanical properties and responsiveness.

Acknowledgements:

We thank Prof. Melany L. Hunt, Prof. Ruby Xiaojing Fu, Dr. Tingtao Zhou, and Jagannadh Boddapati for discussions. W.Z. and C.D. acknowledge support from the Gary Clinard Innovation fund, and the Army Research Office (MURI ARO W911NF-22-2-0109). Computational resources were provided by the High-Performance Computing Center at Caltech. X.X. acknowledges the financial support from Lawrence Livermore National Laboratory's Lab Directed Research and Development Program (22-ERD-004). Work at LLNL was performed under the auspices of the U.S. Department of Energy by Lawrence Livermore National Laboratory under Contract DE-AC52-07NA27344.

Author Contributions Statement:

W.Z. and S.N. contributed equally. W.Z. conceived the idea, designed the structures and fabricated the samples. W.Z., S.N., and C.D. designed the experiments. S.N., W.Z., A.K.P., and P.P. performed the experiments and analyzed experimental data. L.L. performed numerical simulations and analyzed simulation data. X.X. and W.Z. designed the microscale experiments. X.X. and A.G.I. fabricated and tested microscale samples. W.Z. and C.D. wrote the initial draft. All authors interpreted the results and reviewed the manuscript.

Competing Interests Statement:

The authors declare no competing interests.

Figures:

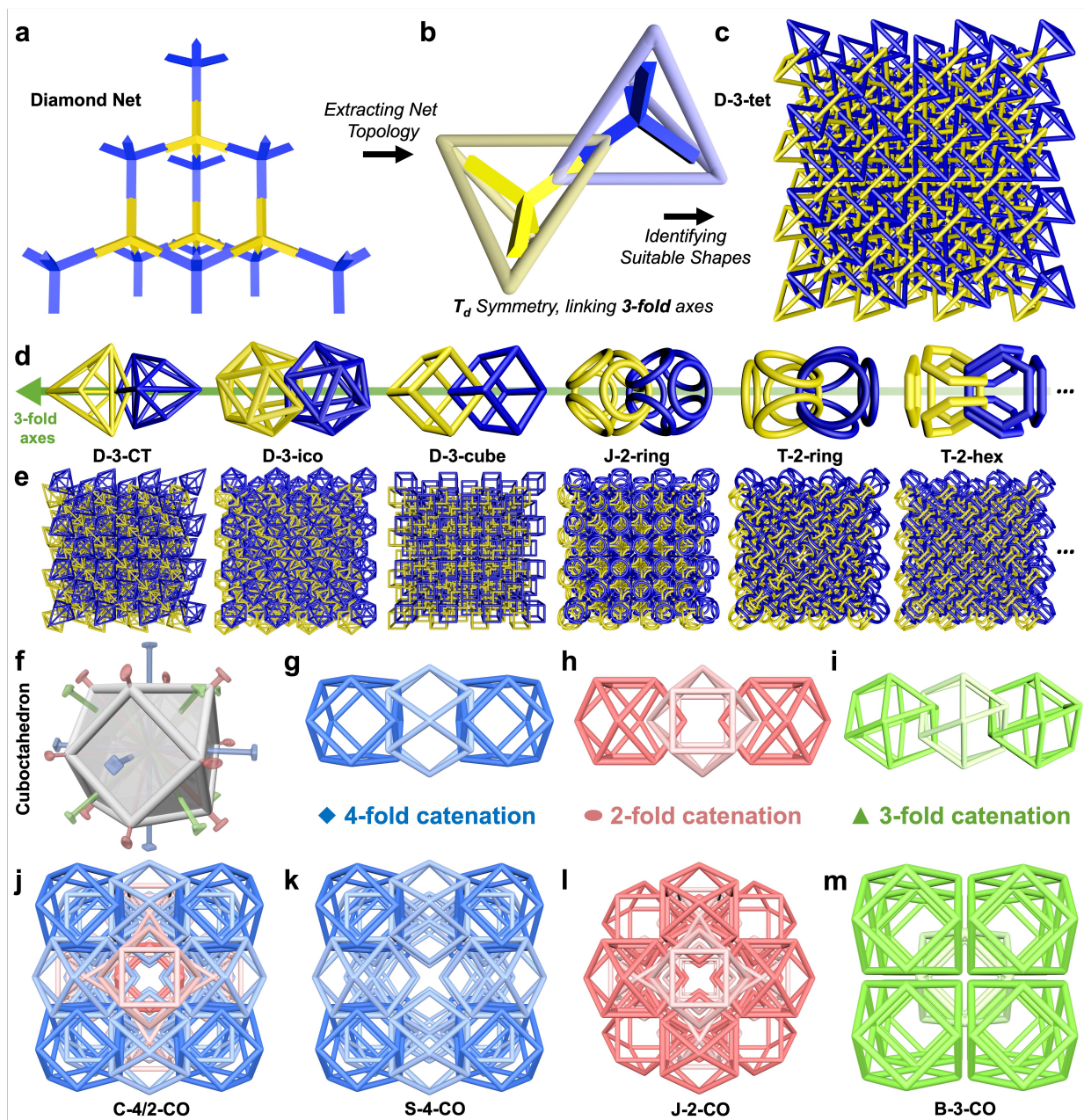


Fig. 1. Design strategy for PAMs. (a-e) A typical design workflow of PAMs from a designated network: (a) Network of the dia topology. (b) Essential nodes and their connections with adjacent nodes in the dia network. Each pair of nodes are mapped with two tetrahedral particles catenating their vertices, while aligning their 3-fold axes. (c) An extended D-3-tet PAM composed of tetrahedral particles. (d) An array of exemplary PAM variants in addition to the catenated tetrahedra, namely Catalan tetrahedra (D-3-CT), icosahedra (D-3-ico), cubes (D-3-cube), octahedrally arranged six-ring clusters (J-2-ring), tetrahedrally arranged four-ring clusters (T-2-

ring), and tetrahedrally arranged four-hexagon clusters (T-2-hex). The green line highlights the 3-fold symmetrical axis. (e) A series of extended PAMs corresponding to the configurations from (d). (f-m) Generation of PAMs from designated particle geometry: (f) A cuboctahedron (CO), catenated through its 4-fold (blue), 3-fold (green), and 2-fold (red) axes. (j-m) Expanded PAMs from the catenations illustrated in (g-h).

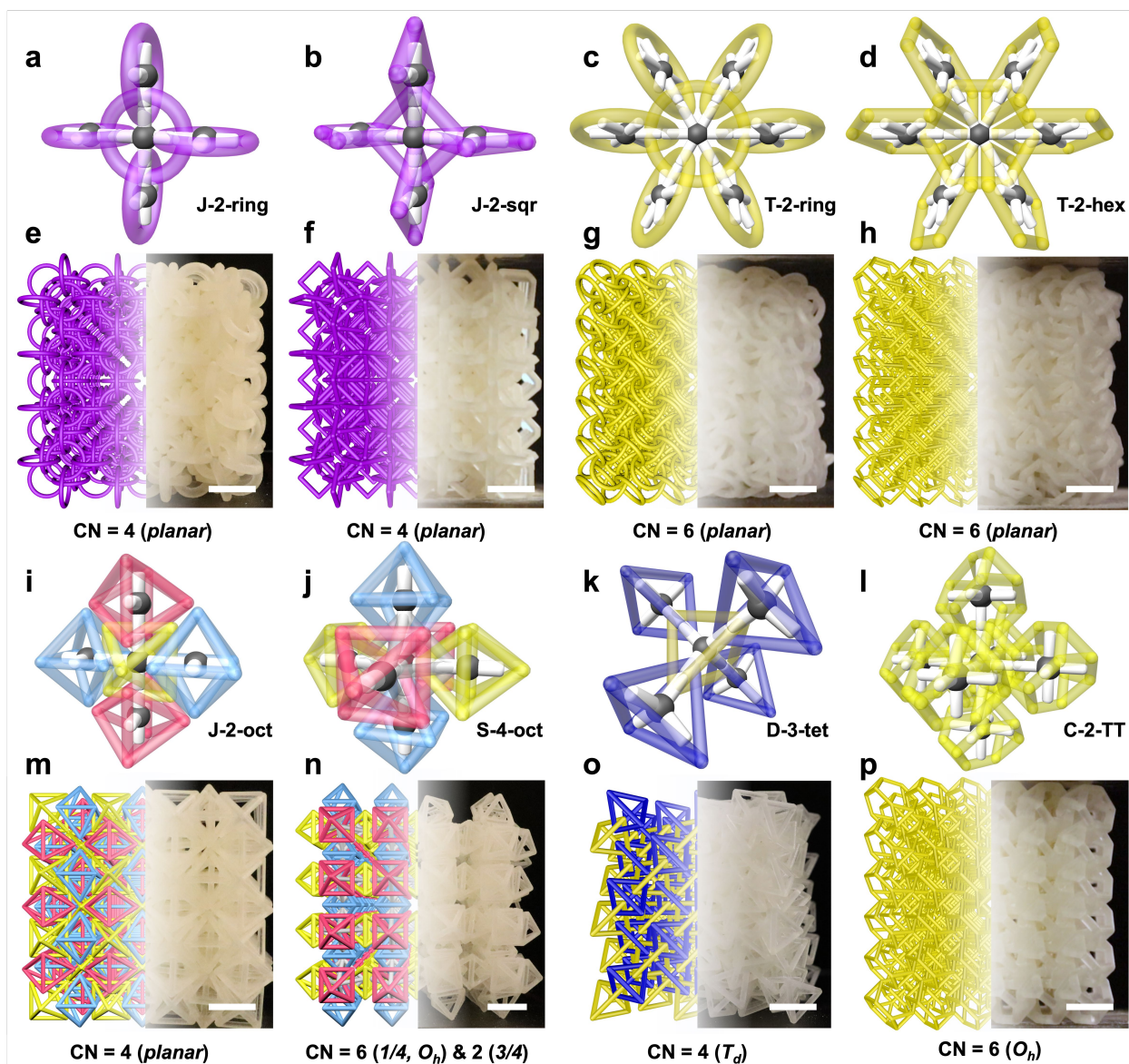


Fig. 2. Catenation configurations and fabrication of PAMs. (a-d) Schematic representations of J-2-ring, J-2-sqr, T-2-ring, and T-2-hex PAMs' local configurations, where J-2-ring and J-2-sqr have planar CN of 4, T-2-ring and T-2-hex have planar CN of 6. (e-h) Illustration and corresponding photos of expanded J-2-ring, J-2-sqr, T-2-ring, and T-2-hex PAM samples. (i-l) Schematic representations of J-2-oct, S-4-oct, D-3-tet, and C-2-TT PAMs' local configurations, where J-2-oct has planar CN of 4, S-4-oct has octahedral (O_h) CN of 6 and 2, D-3-tet has tetrahedral

(T_d) CN of 4, C-2-TT has O_h CN of 6. (m-p) Illustration and corresponding photos of expanded J-2-oct and S-4-oct, D-3-tet, and C-2-TT PAM samples. Scale bars: 1 cm.

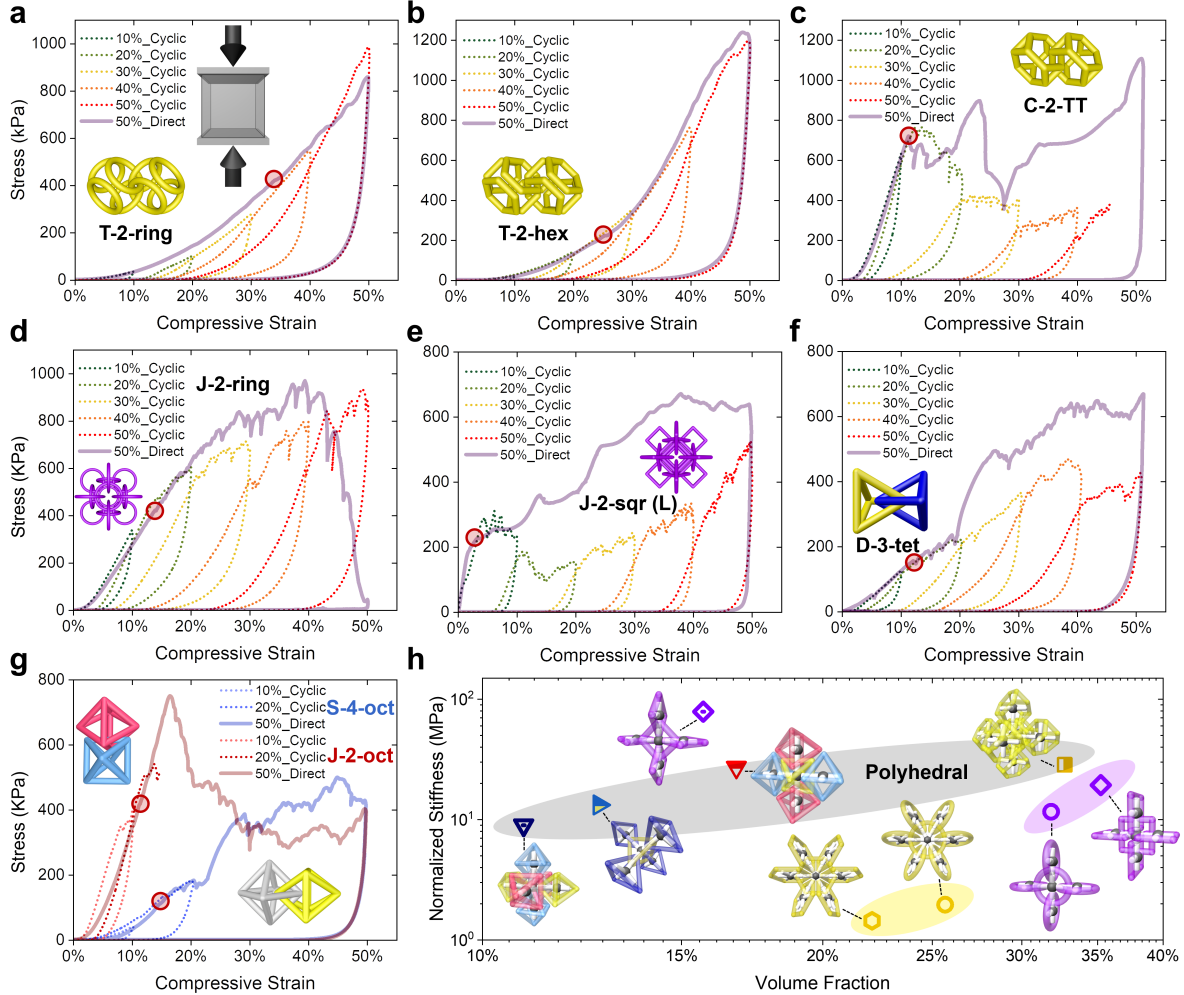


Fig. 3. Uniaxial compression test of PAMs. (a-f) Stress-strain results of six PAMs from cyclic loading (10%, 20%, 30%, 40%, and 50%) and direct loading (50%): (a) T-2-ring, (b) T-2-hex, (c) C-2-TT, (d) J-2-ring, (e) J-2-sqr, and (f) D-3-tet. Red circles indicating the onset of significant fatigue, calculated from first derivative tests. (g) Stress-strain results of J-2-oct and S-4-oct PAMs. (h) Summary of normalized stiffness against measured volume fractions at 5%~10% strain for each PAM.

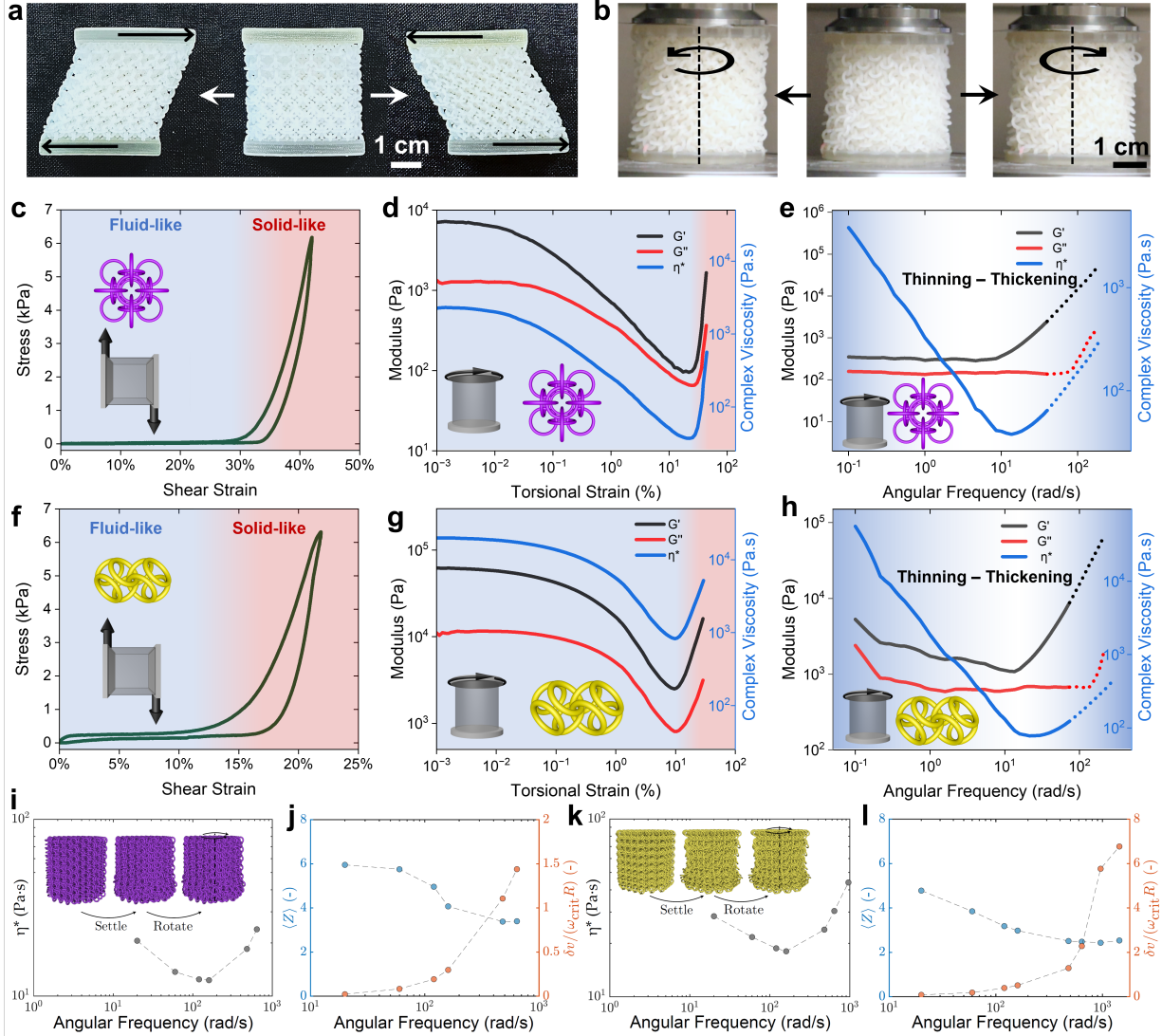


Fig. 4. Shear and rheology test of PAMs. (a, b) PAM samples in shearing and rheological test, showing the deformation in response to corresponding loads. (c, f) Stress-shear strain results for J-2-ring (c) and T-2-ring (f) PAMs, showing the transition from fluid-like to solid-like regime with the increase of shear strain. (d, e, g, h) Rheology results of J-2-ring (d) and T-2-ring (g) PAMs under oscillatory amplitude sweep (e) and frequency sweep (h), with plots of storage modulus (G'), loss modulus (G''), and complex viscosity (η^*) as a function of torsional strain and angular frequency. Dotted lines indicate the region where the tests were significantly affected by the instrument inertia effects. The blue shaded area in (c, d, f, g) indicates the region where the PAMs exhibit fluid-like behavior, transitioning to solid-like behaviors as indicated by the red shaded area. (i, k) Simulation results of the variation of η^* as a function of angular frequency for J-2-ring (i) and T-2-ring (k) cylindrical samples, inset shows the constructed digital twin, which is settled under gravity first and rotated later under a given angular frequency. (j, l) Variations of the average contact number per particle $\langle Z \rangle$ (left axis) and the normalized average particle velocity fluctuation $\frac{\delta v}{w_{crit}R}$ (right axis) as functions of angular frequency, for the T-2 ring sample (j) and the J-2 ring

sample (l), respectively. Above, w_{crit} is the angular frequency at which the inflection of η^* occurs in our simulations and R is the radii of the sample, used only for making δv dimensionless.

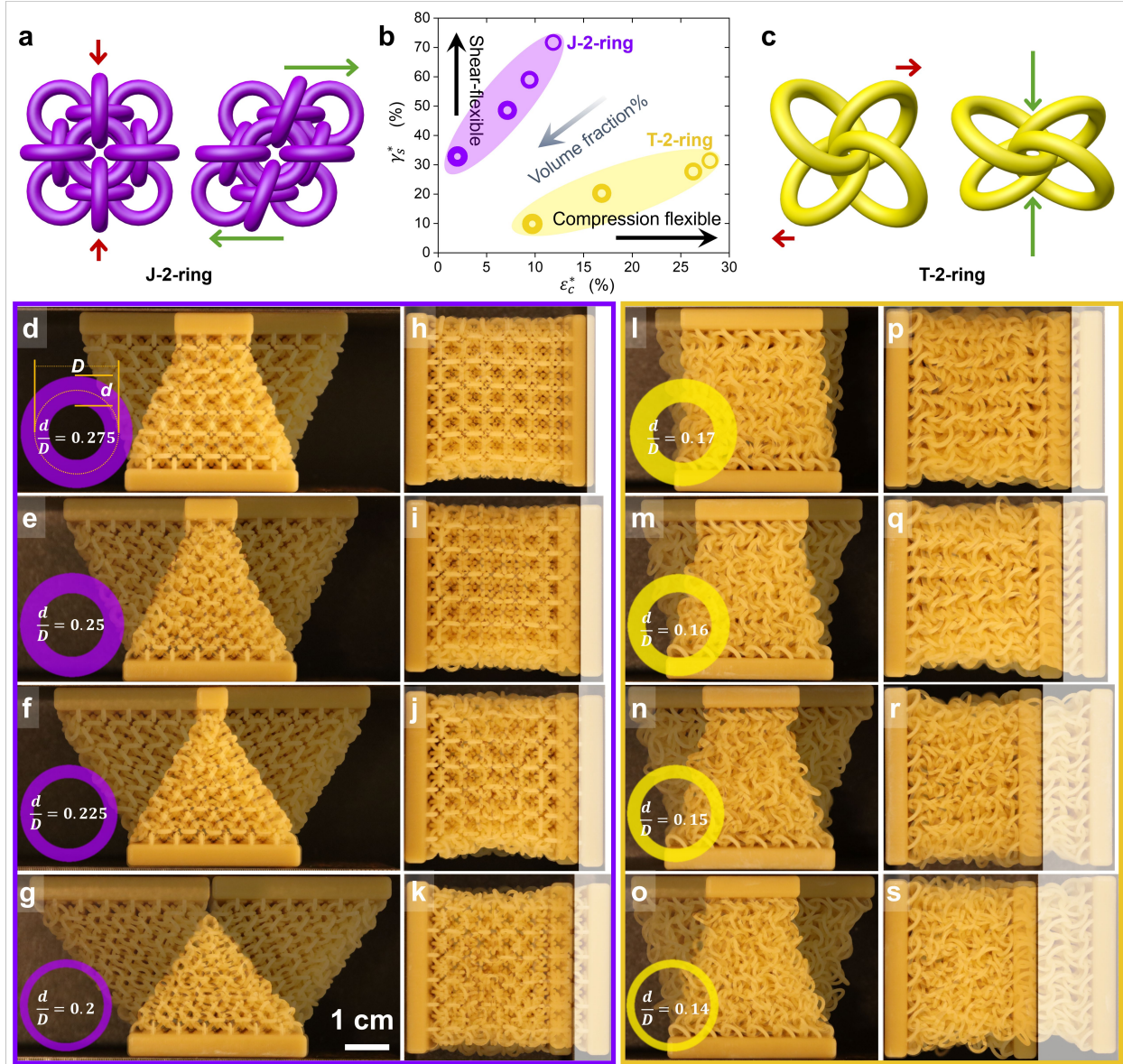


Fig. 5. Programmable critical jamming strains of PAMs. (a, c) The schematics illustrate the local ring arrangements under shearing and compressive loads for J-2-ring and T-2-ring PAMs, respectively. (b) A summary plot displaying critical shear jamming strain (γ_s^*) against the critical compressive jamming strain (ϵ_c^*) for both types of PAMs containing rings with varied thicknesses. (d-s) Photographs showing J-2-ring (d-k) and T-2-ring (l-s) PAMs at their corresponding critical jamming strains.

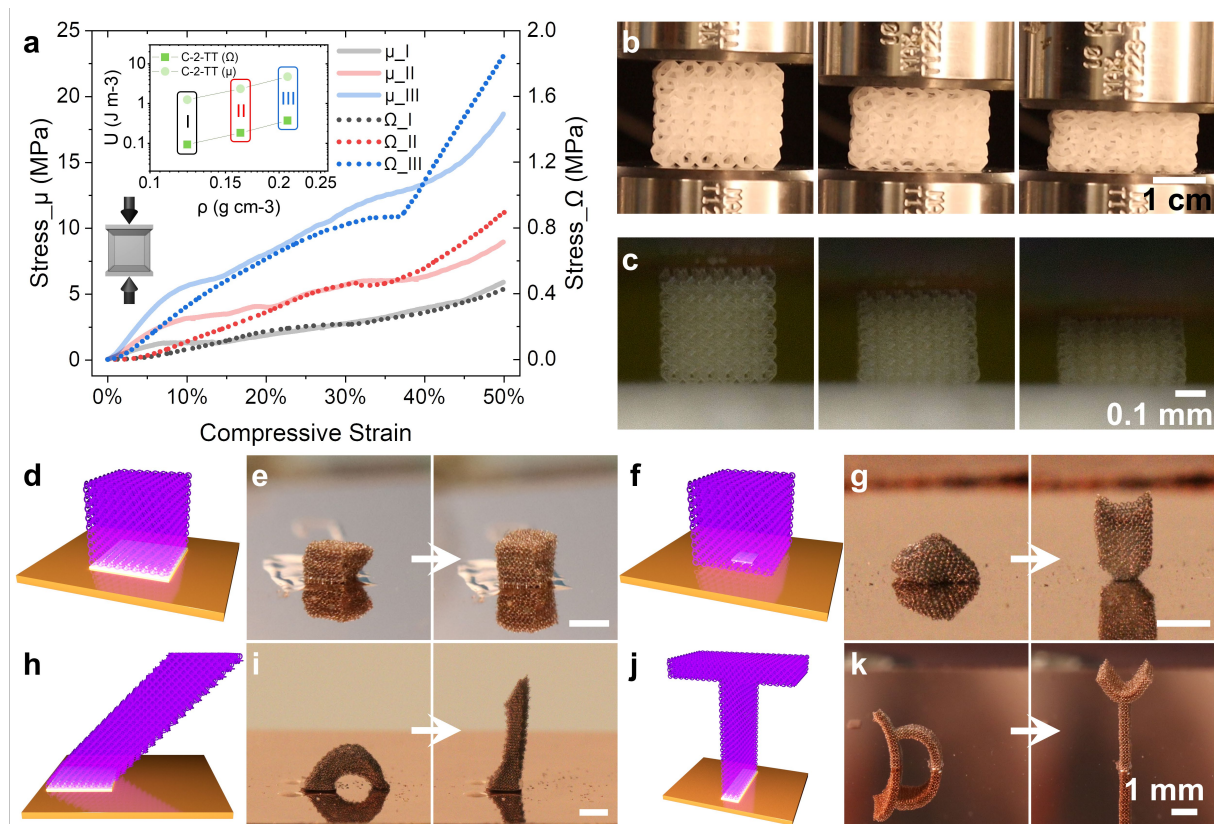


Fig. 6. Scale independence of PAMs and electrostatic actuation of μ -PAMs. (a) Stress-strain curves of C-2-TT PAMs fabricated at different scales (60 times difference in all dimensions) and volume fractions (III>II>I). Inset shows a comparative summary of energy absorption capacities of PAMs at two scales. (b, c) Snapshots of macroscale (b) and microscale (b) C-2-TT PAMs undergoing compression experiments at strains of 0%, 25%, and 50%. Scale bars: 1 cm (b), 0.1 mm (c). (d-g) The J-2-ring μ -PAMs in various geometries including cubes and letters before and after electrostatic expansion. White regions in illustrations highlight the fixing area between the μ -PAMs and the substrate. These μ -PAMs, when subjected to electrostatic charges generated by a Van de Graaff generator, deploy from a relaxed natural state to an expanded state due to inter-particle electrostatic repulsion. Scale bars: 1 mm.

References:

1. Zheng, X. *et al.* Ultralight, ultrastiff mechanical metamaterials. *Science* **344**, 1373–1377 (2014).
2. Kadic, M., Milton, G. W., van Hecke, M. & Wegener, M. 3D metamaterials. *Nat. Rev. Phys.* **1**, 198–210 (2019).
3. Lakes, R. Foam Structures with a Negative Poisson's Ratio. *Science* **235**, 1038–1040 (1987).
4. Babaei, S. *et al.* 3D soft metamaterials with negative Poisson's ratio. *Adv. Mater* **25**, 5044–5049 (2013).
5. Frenzel, T., Kadic, M. & Wegener, M. Three-dimensional mechanical metamaterials with a twist. *Science* **358**, 1072–1074 (2017).
6. Boddapati, J., Flaschel, M., Kumar, S., De Lorenzis, L. & Daraio, C. Single-test evaluation of directional elastic properties of anisotropic structured materials. *J. Mech. Phys. Solids* **181**, 105471 (2023).
7. Kadic, M., Bückmann, T., Stenger, N., Thiel, M. & Wegener, M. On the practicability of pentamode mechanical metamaterials. *Appl. Phys. Lett.* **100**, (2012).
8. Bückmann, T., Thiel, M., Kadic, M., Schittny, R. & Wegener, M. An elasto-mechanical unfeelability cloak made of pentamode metamaterials. *Nat. Commun.* **5**, 4130 (2014).
9. Shaikeea, A. J. D., Cui, H., O'Masta, M., Zheng, X. R. & Deshpande, V. S. The toughness of mechanical metamaterials. *Nat. Mater.* **21**, 297–304 (2022).
10. Xue, R. *et al.* Mechanical design and energy absorption performances of novel dual scale hybrid plate-lattice mechanical metamaterials. *Extrem. Mech. Lett.* **40**, 100918 (2020).
11. Davami, K. *et al.* Ultralight shape-recovering plate mechanical metamaterials. *Nat. Commun.* **6**, 10019 (2015).
12. Al-Ketan, O., Soliman, A., AlQubaisi, A. M. & Abu Al-Rub, R. K. Nature-inspired lightweight cellular co-continuous composites with architected periodic gyroidal structures. *Adv. Eng. Mater.* **20**, 1700549 (2018).
13. Al-Ketan, O. & Abu Al-Rub, R. K. Multifunctional mechanical metamaterials based on triply periodic minimal surface lattices. *Adv. Eng. Mater.* **21**, 1900524 (2019).
14. Ganghoffer, J.-F., Wazne, A. & Reda, H. Frontiers in homogenization methods towards generalized continua for architected materials. *Mech. Res. Commun.* **130**, 104114 (2023).
15. Arabnejad, S. & Pasini, D. Mechanical properties of lattice materials via asymptotic homogenization and comparison with alternative homogenization methods. *Int. J. Mech. Sci.* **77**, 249–262 (2013).
16. Liu, K., Sun, R. & Daraio, C. Growth rules for irregular architected materials with programmable properties. *Science* **377**, 975–981 (2022).

17. Zaiser, M. & Zapperi, S. Disordered mechanical metamaterials. *Nat. Rev. Phys.* **5**, 679–688 (2023).
18. Florijn, B., Coulais, C. & van Hecke, M. Programmable Mechanical Metamaterials. *Phys. Rev. Lett.* **113**, 175503 (2014).
19. Bertoldi, K., Vitelli, V., Christensen, J. & van Hecke, M. Flexible mechanical metamaterials. *Nat. Rev. Mater.* **2**, 17066 (2017).
20. Coulais, C., Sabbadini, A., Vink, F. & van Hecke, M. Multi-step self-guided pathways for shape-changing metamaterials. *Nature* **561**, 512–515 (2018).
21. Xia, X. *et al.* Electrochemically reconfigurable architected materials. *Nature* **573**, 205–213 (2019).
22. Xia, X., Spadaccini, C. M. & Greer, J. R. Responsive materials architected in space and time. *Nat. Rev. Mater.* **7**, 683–701 (2022).
23. Shan, S. *et al.* Multistable architected materials for trapping elastic strain energy. *Adv. Mater* **27**, 4296–4301 (2015).
24. Haghpanah, B., Salari-Sharif, L., Pourrajab, P., Hopkins, J. & Valdevit, L. Multistable shape-reconfigurable architected materials. *Adv. Mater* **28**, 7915–7920 (2016).
25. Li, S., Fang, H., Sadeghi, S., Bhowad, P. & Wang, K. Architected origami materials: how folding creates sophisticated mechanical properties. *Adv. Mater.* **31**, 1805282 (2019).
26. Liu, J. *et al.* Harnessing buckling to design architected materials that exhibit effective negative swelling. *Adv. Mater* **28**, 6619–6624 (2016).
27. Estrin, Y., Dyskin, A. V & Pasternak, E. Topological interlocking as a material design concept. *Mater. Sci. Eng. C* **31**, 1189–1194 (2011).
28. Chong, C., Porter, M. A., Kevrekidis, P. G. & Daraio, C. Nonlinear coherent structures in granular crystals. *J. Phys. Condens. Matter* **29**, 413003 (2017).
29. Karuriya, A. N. & Barthelat, F. Granular crystals as strong and fully dense architected materials. *Proc. Natl. Acad. Sci.* **120**, e2215508120 (2023).
30. Wang, Y., Li, L., Hofmann, D., Andrade, J. E. & Daraio, C. Structured fabrics with tunable mechanical properties. *Nature* **596**, 238–243 (2021).
31. Tang, P., Coros, S. & Thomaszewski, B. Beyond Chainmail: Computational Modeling of Discrete Interlocking Materials. *ACM Trans. Graph.* **42**, 1–12 (2023).
32. Carlucci, L., Ciani, G. & Proserpio, D. M. Polycatenation, polythreading and polyknotting in coordination network chemistry. *Coord. Chem. Rev.* **246**, 247–289 (2003).
33. Liu, Y., O’Keeffe, M., Treacy, M. M. J. & Yaghi, O. M. The geometry of periodic knots, polycatenanes and weaving from a chemical perspective: A library for reticular chemistry. *Chem. Soc. Rev.* **47**, 4642–4664 (2018).
34. O’Keeffe, M. & Treacy, M. M. J. Embeddings of Graphs: Tessellate and Decussate Structures. *Int.*

- J. Topol.* **1**, 1–10 (2024).
35. Ma, T. *et al.* Catenated covalent organic frameworks constructed from polyhedra. *Nat. Synth.* **2**, 286–295 (2023).
 36. Meng, W. *et al.* An elastic metal–organic crystal with a densely catenated backbone. *Nature* **598**, 298–303 (2021).
 37. RCSR. <https://rcsr.anu.edu.au/>.
 38. Turner, M. Ball and stick models for organic chemistry. *J. Chem. Educ.* **48**, 407 (1971).
 39. Grima, J. N. & Evans, K. E. Auxetic behavior from rotating squares. *J. Mater. Sci. Lett.* **19**, 1563–1565 (2000).
 40. Mullins, L. Effect of stretching on the properties of rubber. *Rubber Chem. Technol.* **21**, 281–300 (1948).
 41. Peña, E. Prediction of the softening and damage effects with permanent set in fibrous biological materials. *J. Mech. Phys. Solids* **59**, 1808–1822 (2011).
 42. Murphy, K. A., Dahmen, K. A. & Jaeger, H. M. Transforming mesoscale granular plasticity through particle shape. *Phys. Rev. X* **9**, 11014 (2019).
 43. Güden, M., Çelik, E., Hızal, A., Altındış, M. & Çetiner, S. Effects of compaction pressure and particle shape on the porosity and compression mechanical properties of sintered Ti6Al4V powder compacts for hard tissue implantation. *J. Biomed. Mater. Res. Part B Appl. Biomater.* **85B**, 547–555 (2008).
 44. de Goede, T. C., de Bruin, K. G. & Bonn, D. High-velocity impact of solid objects on Non-Newtonian Fluids. *Sci. Rep.* **9**, 1250 (2019).
 45. Kawamoto, R., Andò, E., Viggiani, G. & Andrade, J. E. Level set discrete element method for three-dimensional computations with triaxial case study. *J. Mech. Phys. Solids* **91**, 1–13 (2016).
 46. Kawamoto, R., Andò, E., Viggiani, G. & Andrade, J. E. All you need is shape: Predicting shear banding in sand with LS-DEM. *J. Mech. Phys. Solids* **111**, 375–392 (2018).
 47. Li, L., Marteau, E. & Andrade, J. E. Capturing the inter-particle force distribution in granular material using LS-DEM. *Granul. Matter* **21**, 1–16 (2019).
 48. Lun, C. K. K., Savage, S. B., Jeffrey, D. J. & Chepurniy, N. Kinetic theories for granular flow: inelastic particles in Couette flow and slightly inelastic particles in a general flowfield. *J. Fluid Mech.* **140**, 223–256 (1984).
 49. Da Cruz, F., Emam, S., Prochnow, M., Roux, J.-N. & Chevoir, F. Rheophysics of dense granular materials: Discrete simulation of plane shear flows. *Phys. Rev. E* **72**, 21309 (2005).
 50. Li, L. & Andrade, J. E. Identifying spatial transitions in heterogenous granular flow. *Granul. Matter* **22**, 52 (2020).

Methods:

Materials and Fabrication of Macroscopic PAMs

PAM samples were fabricated using additive manufacturing from 3D Systems employing the Multi Jet Fusion fabrication process, sourced from a commercial 3D printing service (Shapeways). Materials used in this study are Visijet M3, M2R-Clear, and M2R-TN. All mechanical tests were conducted using PAMs fabricated using Visijet M3. Visijet M3 has a density of 1.02 g/cm^3 , a tensile modulus of 1463 MPa, and a tensile strength of 42.4 MPa^{51} . Upon receiving the samples, some had remaining supporting wax materials, which could (i) alter the particle geometries and (ii) limit particles' DOFs. These wax materials can be selectively dissolved by soaking the samples in isopropanol solution for 2 min at a temperature between 40 and 60 °C. All PAM samples were manually checked to ensure no remaining particle agglutination before mechanical characterizations. To test PAM samples under shear loading (in simple shear and rheology tests), we incorporated two solid gripping plates in the sample's design and fabrication (Extended Data Fig. 3). The plates partially overlapped with the particles at the top and bottom surfaces and were used to mount the samples to the loading grips and distribute the load uniformly across all particles on the surfaces.

Quasi-static Compression and Shear Tests

Quasi-static uniaxial compression and simple shear experiments were conducted using an Instron ElectroPuls E3000 universal testing machine. This testing machine was equipped with an ATI Mini85 multi-axial Force/Torque sensor capable of measuring both force and torque along three mutually perpendicular axes. The load cell's capacity was 1.9 kN and 3.8 kN for force measurements in the X, Y, and Z directions respectively, and 80 Nm for torque measurement along all three axes. For the quasi-static compression trials, cubic specimens were carefully positioned between the compression platens. The orientation ensured that the centerline of the specimen was aligned with the centerline of the load cell. To mount the shear test specimens in the Instron machine, a pair of custom-designed mounting plates was affixed to the solid gripping plates (3D-printed alongside the specimen). The specimens were oriented such that the solid gripping plates aligned with the sides of the specimen. Each mounting plate was subsequently connected to the corresponding upper and lower parts of the tensile grip in the Instron. This modification transformed the uniaxial tensile/compression test apparatus into a configuration suitable for simple shear testing. The force-displacement responses of all specimens were recorded during quasi-static compression tests, at a displacement-controlled loading rate of 0.1/s, to maintain experimental consistency. In the compression tests, a series of multiple compression cycles were performed on a single specimen, each with a varying maximum loading strain spanning from 10% to 50%. Due to the inherently stochastic nature of PAMs, their dimensions exhibited variability in each instance, influenced by random internal arrangement patterns. Thus, dimensions of relaxed PAMs under gravity were measured multiple times, across various regions. The resultant average measurements were then utilized to compute effective stress and strain, accounting for this variability.

Rheology Tests

The dynamic oscillatory rheological tests were performed using a torque-controlled Discovery HR20 Hybrid Rheometer, from TA Instruments which has axial force and torque limits of 50 N and 0.2 Nm with sensitivities at 0.005 N and 10^{-10} Nm, respectively. The experiment was carried

out using a 40 mm diameter parallel plate tool, maintaining a constant temperature of 25 °C and a frequency of 0.5 Hz, with the torsional strain ranging from 10⁻⁶ % to 100%. Cylindrical specimens of original height and diameter of 40 mm were employed. These specimens were designed with thin solid components at both ends, strategically incorporated to ensure steadfast attachment to the rheometer and prevent any slippage. To achieve this secure attachment, thin, robust double-sided adhesive tapes were utilized. Torsional rotation was applied to the specimen through the upper parallel plate, while the bottom side remained securely fixed. Data acquisition was facilitated using the TRIOS software. Data points lying within the strain range of 10⁻⁶ % to 10⁻³ %, were subjected to noise interference and were deliberately excluded from the study.

Numerical Simulation of rheological experiments (LS-DEM)

Numerical frequency sweep experiments were conducted using LS-DEM. The model parameters, as well as the construction of digital twins, follows those reported in a previous work³⁰ where LS-DEM was utilized to study the tunable mechanics of structured fabrics. The inter-particle friction for the J-2-ring was set as 0.25, same as in the previous work³⁰. The inter-particle friction for the T-2-ring sample was increased to 0.5, to partially account for the noticeable surface roughness of the 3D-printed ring particles.

Each numerical experiment consists of two steps: settling under gravity until equilibrium and rotating under a given angular frequency. Note that, rings in the bottom layer were fixed during both steps, while those in the top layer were fixed during the first step and were rotated with respect to the sample's vertical central axis during the second step. The rotation in the second step was imposed according to an applied sinusoidal shear strain $\gamma(t) = A\sin(\omega t)$, where A is the amplitude (set at 0.1 for all simulations) and ω is the angular frequency. By doing so, we resemble as close as possible the experimental loading conditions. In practice, the rotation angle $\theta(t)$ and the speed $\dot{\theta}(t)$ were calculated, from which the spatial position, orientation, as well as translational and angular velocity of each ring in the top layer (which revolves around the rotation axis) can be determined. $\theta(t)$ and $\dot{\theta}(t)$ were calculated according to the following two expressions:

$$\theta(t) = \frac{YH}{R} A\sin(\omega t),$$

$$\dot{\theta}(t) = \frac{YH}{R} A\omega\cos(\omega t).$$

Above, H is the height and R is the radius of the cylindrical sample, determined from the sample's settled configuration. As rings in the top layer were moved via the imposed motion described above, the torque they felted, $T(t)$, was computed. This is done by summing the cross products between the positions of them (with respect to the rotation axis) and the contact forces (projected onto the plane perpendicular to the rotation axis) felted by them. The shear stress $\tau(t)$ was then computed according to the following expression:

$$\tau(t) = \frac{T(t)R}{J},$$

where $J = \frac{\pi R^4}{2}$ is the polar moment of inertia of the sample (treated as a rigid cylinder). The maximum value τ_{\max} was then determined from $\tau(t)$ and was used to find the complex viscosity η^* based on the following expression:

$$\eta^* = \frac{\tau_{\max}}{A\omega}.$$

For each simulation with a given angular frequency, we can get multiple values of τ_{\max} , thereby calculating multiple values for η^* . These values were averaged, and the mean values were reported in the main text. Variations of η^* due to variations in τ_{\max} were found to be small (one order of magnitude smaller) compared to the mean value of η^* and are therefore not reported in the main text. For this work, the number of τ_{\max} value varied from two to ten depends on the imposed angular frequency and out of consideration of computational costs. In general, the larger the angular frequency, the cheaper (in terms of computational cost) the simulation becomes for getting more values for τ_{\max} .

At each location where τ_{\max} is computed, we also compute the mean contact number per particle $\langle Z \rangle$ and the mean particle velocity fluctuation δv by averaging all particles in a sample. The former is easy to get directly from our LS-DEM simulation outputs. For the latter, we take the particle velocity output and perform a spatial average to get δv . Here, we consider δv along the azimuth direction only, and we partition particles into different layers vertically (z_i , with z being the height coordinate location) and different annular bins (r_j , with r being the radial coordinate location) within each layer. Then, δv is computed as:

$$\delta v = \frac{1}{N_z} \sum_{i=1}^{N_z} \frac{1}{N_r} \sum_{j=1}^{N_r} \langle \delta v \rangle_{z_i r_j},$$

where N_z and N_r is the number of layers and bins per layer, respectively. $\langle \delta v \rangle_{z_i r_j}$ is the particle-averaged velocity fluctuation associated with a particular bin in a given layer, and it is computed as the root square of the granular temperature $\langle T \rangle_{z_i r_j}$:

$$\langle \delta v \rangle_{z_i r_j} = \sqrt{\langle T \rangle_{z_i r_j}},$$

$$\text{with } \langle T \rangle_{z_i r_j} = \frac{1}{N_{p,z_i r_j}} \sum_{k=1}^{N_{p,z_i r_j}} (v_{k,r} - \langle v_{k,r} \rangle)^2.$$

Above, $N_{p,z_i r_j}$ is the number of particles residing in that considered bin. Within this bin, $v_{k,r}$ is the projected velocity along the azimuth direction of the k -th particle:

$$v_{k,r} = \vec{v}_k \cdot \vec{t}_k,$$

where \vec{v}_k is the velocity vector of the k -th particle and \vec{t}_k is the tangential unit vector along the azimuth direction associated with that particle. Lastly, $\langle v_{k,r} \rangle$ is the mean projected velocity, computed as the following:

$$\langle v_{k,r} \rangle = \frac{1}{N_p} v_{k,r}, \text{ where we drop the } z_i \text{ and } r_j \text{ subscripts for simplicity.}$$

Fabrication and Characterization of Microscopic PAMs

The μ -PAM samples were fabricated by two-photon lithography using a commercial 3D printer (Nanoscribe GT2) and a commercial resin (Nanoscribe IP-S). The smaller samples used in micro-mechanical compression experiments were printed as designed, without adding additional mechanical supports. The larger samples used in electrostatic deployment experiments were

printed by stitching multiple segments sequentially due to the limited field of view of the 25X objective used for two-photon lithography. To prevent drifting issues of the interlocked but unsupported structures due to the prolonged printing time for larger μ -PAM structures, we incorporated additional support structures (body-centered cubic lattices with lateral beam thickness of 500 nm) that overlapped with the μ -PAM lattices in the CAD design. The combined geometry was printed simultaneously so that the body-centered cubic scaffold provided additional support and confinement of the PAM during the printing process. The as-printed samples were immersed in propylene glycol methyl ether acetate (Sigma-Aldrich) for 1hr and then in isopropanol for 1hr to rinse off the remaining uncured liquid resin. The cleaned samples were dried in air. The larger samples used in electrostatic deployment experiments were etched in a PIE Scientific Tergeo Plus Plasma Cleaner for 10-20 h (direct mode, oxygen flow rate 10 sccm, Ar flow rate 30 sccm, RF power 30 W, pulse duty cycle 50/255), to remove the supporting scaffold. Special attention was paid to increase uniformity of etching for all polymer surfaces so that the 500 nm thick body-centered cubic supporting lattices could be removed before substantially damaging the μ -PAM structure. A Keyence VHX-7000 Digital Microscope was used to inspect the etched μ -PAM samples every hour to complete removal of the supporting lattice and release of the interlocked particles in the polycatenated architecture.

For electrostatic deployment experiments, the fully released μ -PAM samples attached to ITO-coated glass substrates were coated with nominally 300 nm thick of Cu (measured on a planar substrate) using a Kurt Lesker PRO Line PVD 75 thin film sputtering system at 100 W DC power. The Cu-coated samples were attached to a Lethan Corporation Van De Graaff Generator using double-sided conductive Cu tapes. Digital photos and videos were taken when the Van De Graaff generator was being turned on and off.

For microscale mechanical testing experiments, the μ -PAMs were fabricated on 5 mm-by-5 mm Si substrates directly without the additional supporting scaffold. The uniaxial compression tests were conducted using a displacement-controlled micromechanical testing system (Kamrath Weiss Tensile & Compression Module). The device was equipped with custom compression grips, including an alumina flat punch with a tip of 2 mm in diameter, a load cell of 10N, and a 3D-printed fixture to facilitate accurate and convenient mounting of the 5 mm Si substrates onto the compression module. Samples were tested at a strain rate of 0.5%/s. The experiments were performed under a Keyence VHX-7000 digital microscope for in situ video recording.

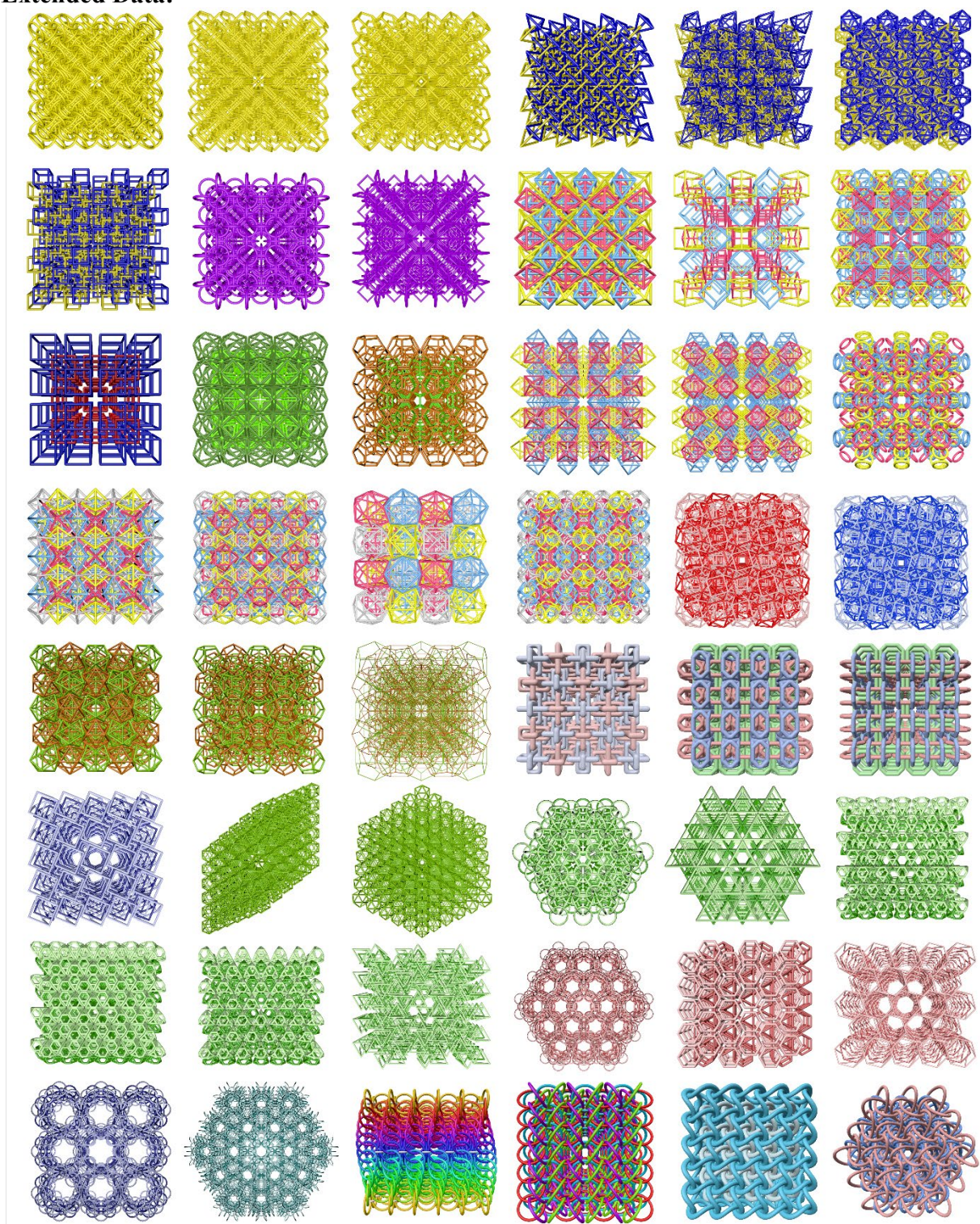
Method-only References:

51. Shapeways. <https://www.shapeways.com/materials/fine-detail-plastic-3>.

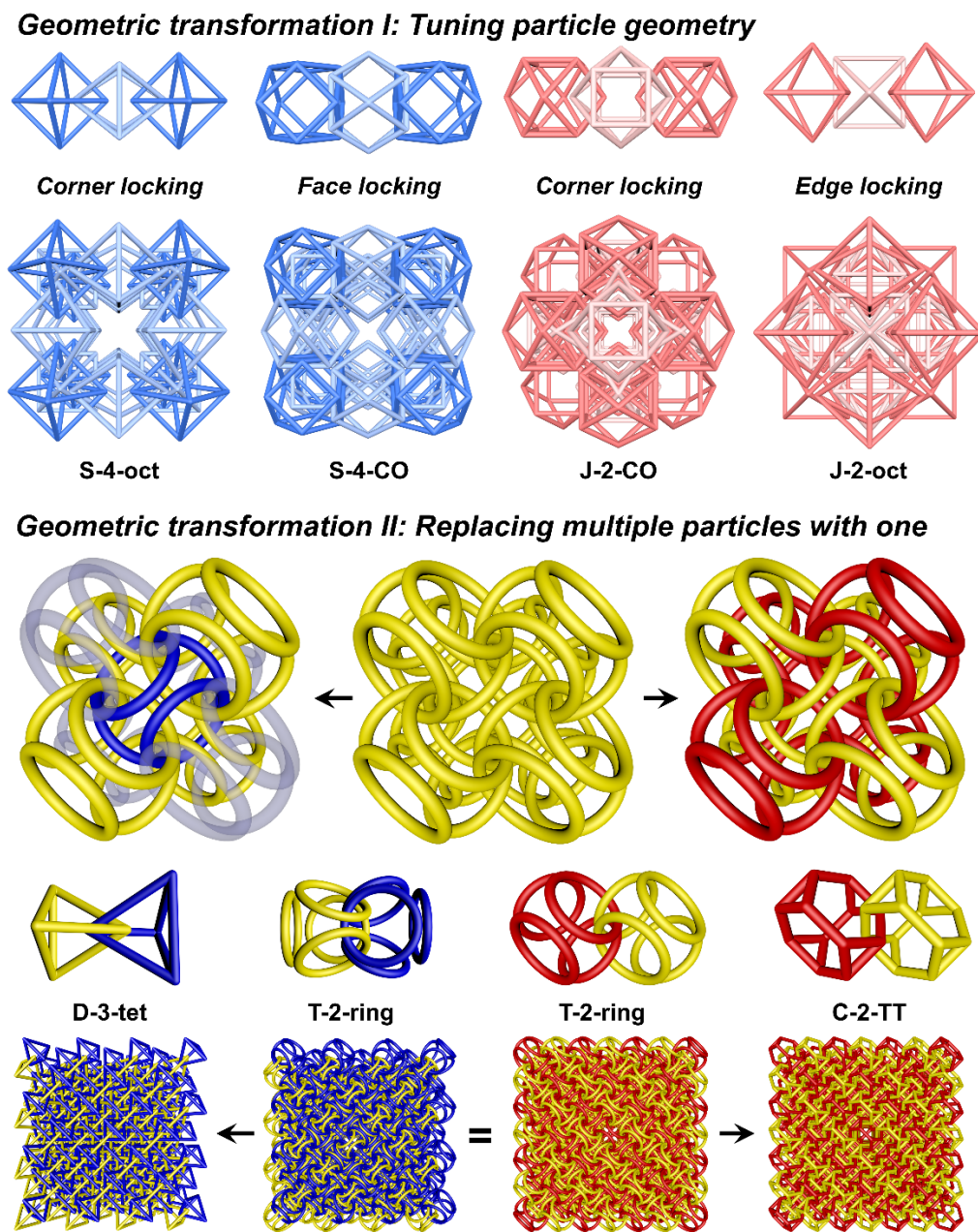
Data Availability:

The data that support the findings of this study are available from the corresponding author upon reasonable request.

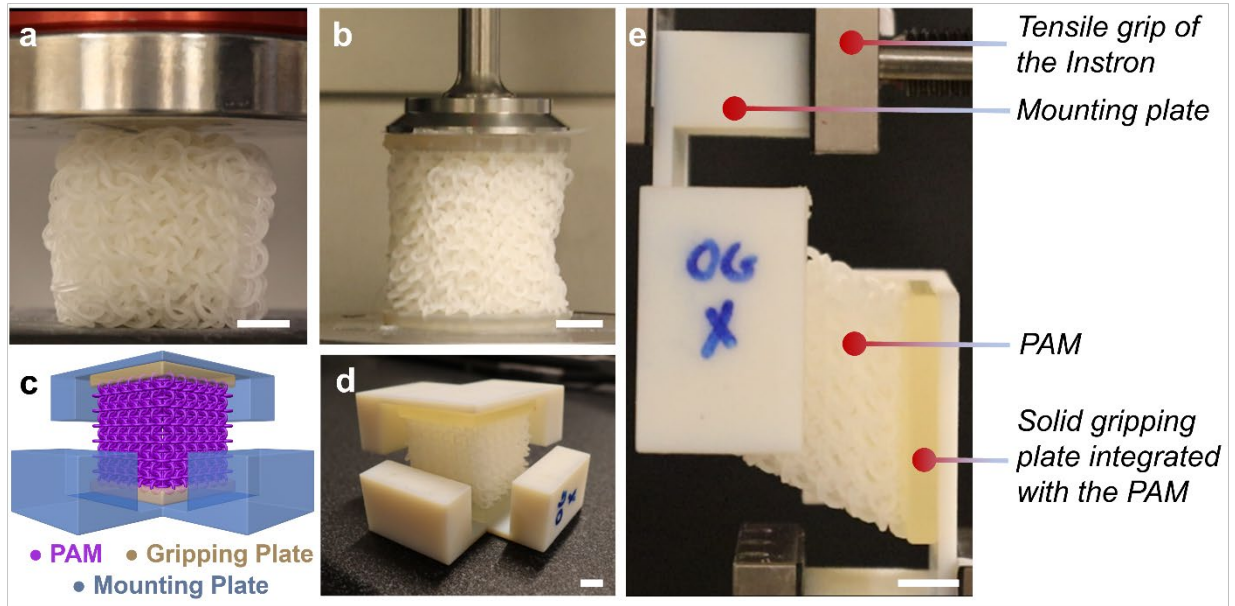
Extended Data:



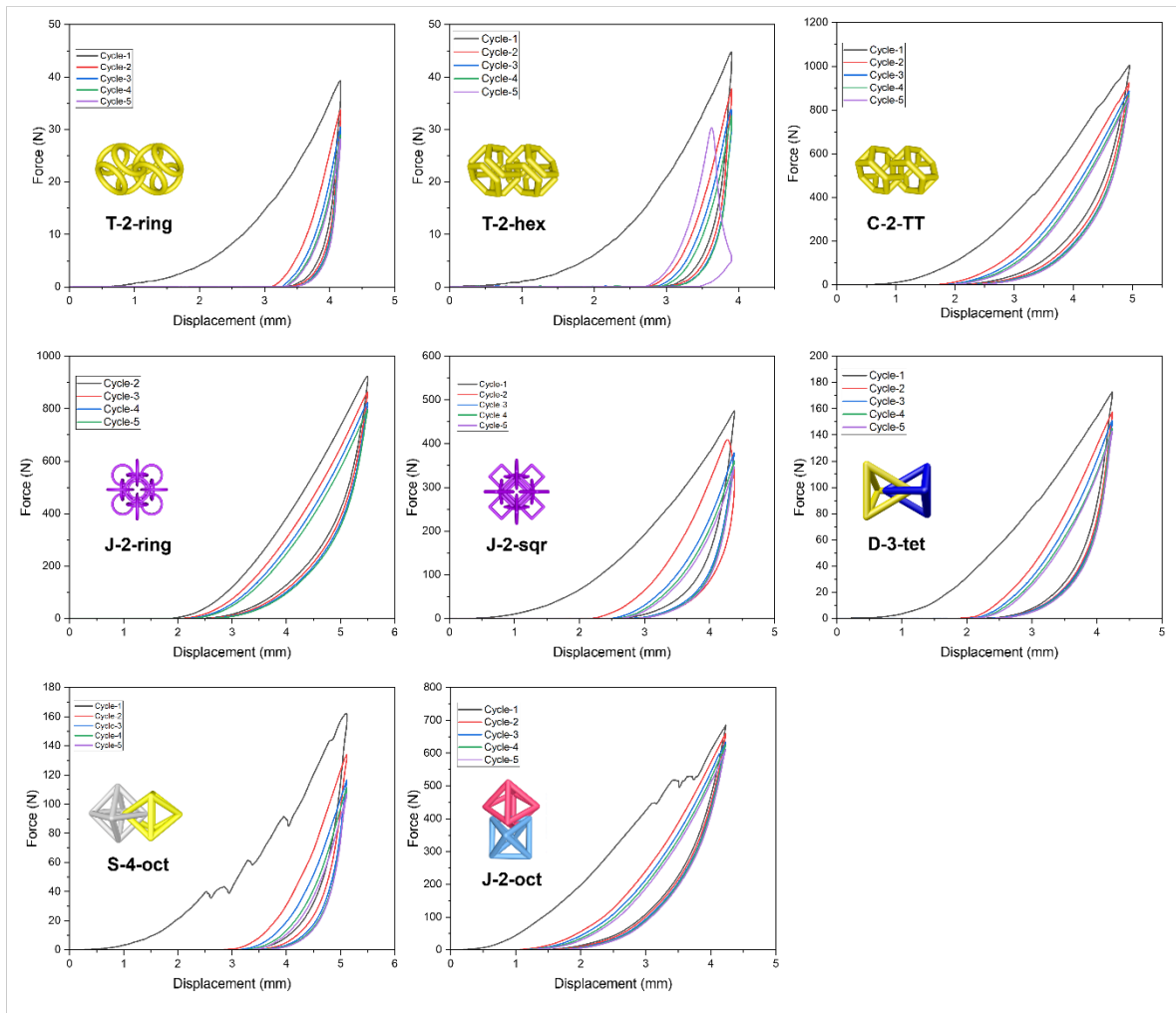
Extended Data Fig. 1. Selected library of PAMs composed of single type of particles. Different colors highlight local structural features that may be visually challenging to distinguish, including particle geometries, orientations, and linking types. PAMs consist of more than one types of particles are not listed in this library.



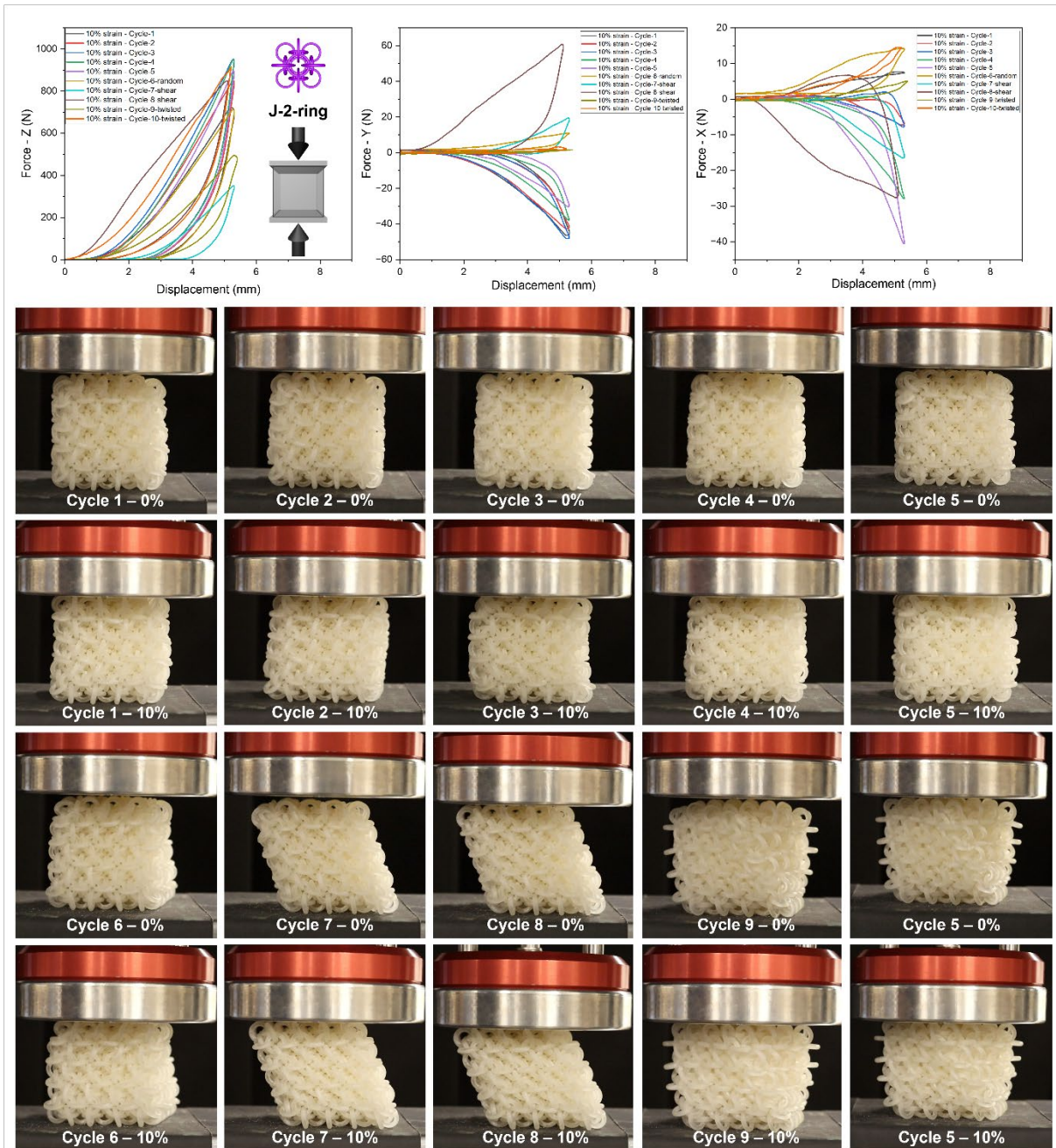
Extended Data Fig. 2. Geometric transformations of PAMs. (I) Tuning particle geometry of PAMs with the same topology. PAMs composed of octahedral and cuboctahedral particles are linked in S-4 and J-2 topologies. By truncating octahedra into cuboctahedra, existing local contact mechanisms of PAMs can be drastically altered, namely transitioning from corner-to-corner locking into face-to-face locking or edge-to-edge locking. (II) Replacing multiple particles with one (geometric transformations among T-2-ring, D-3-tet, and C-2-TT). On the left side, T-2-ring is divided into two sets of tetrahedral clusters (yellow and blue), arranged in a dia topology. Replacing each cluster with one tetrahedral particle results in a D-3-tet. On the right side, T-2-ring is divided into two sets of tetrahedral clusters (yellow and red), arranged in a pcu topology. Replacing each cluster with one truncated tetrahedral particle results in a C-2-TT.



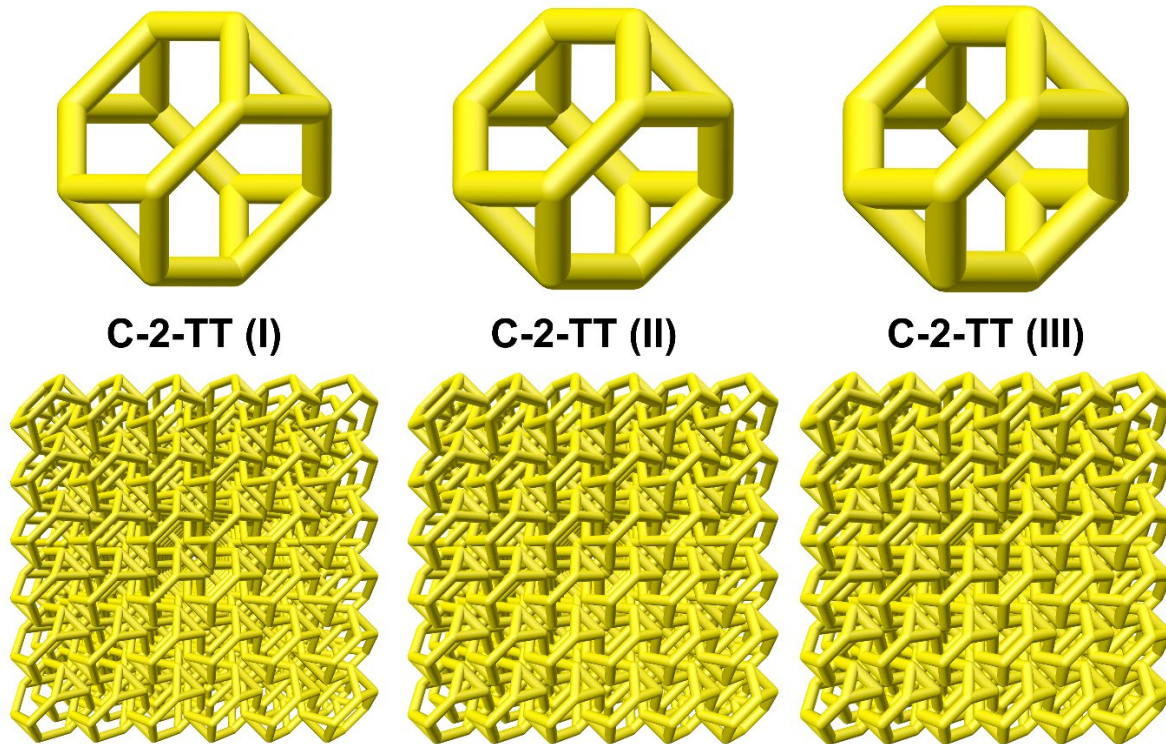
Extended Data Fig. 3. Experimental setups for mechanical characterizations. (a) Uniaxial compression test setup, (b) Rheology test setup, (c) Design and positioning of the mounting plate on the PAM specimen to secure the shear test sample in the Instron testing machine, (d) Assembly of the mounting plate with the solid gripping plate integrated into the shear test specimen, and (e) Shear test specimen positioned in the Instron machine utilizing the solid gripping plate and mounting plate. Scale bars: 1 cm.



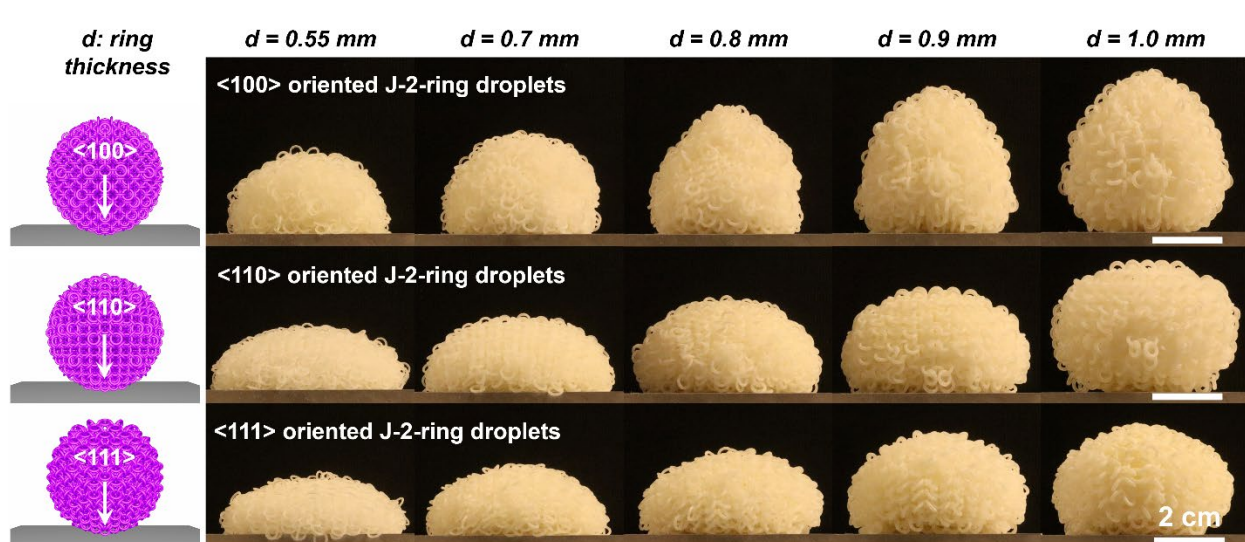
Extended Data Fig. 4. Cyclic compression of all PAMs at same loading conditions (10% strain). A series of force-displacement response from cyclic compression tests on all discussed PAMs in this study at 10% strains.



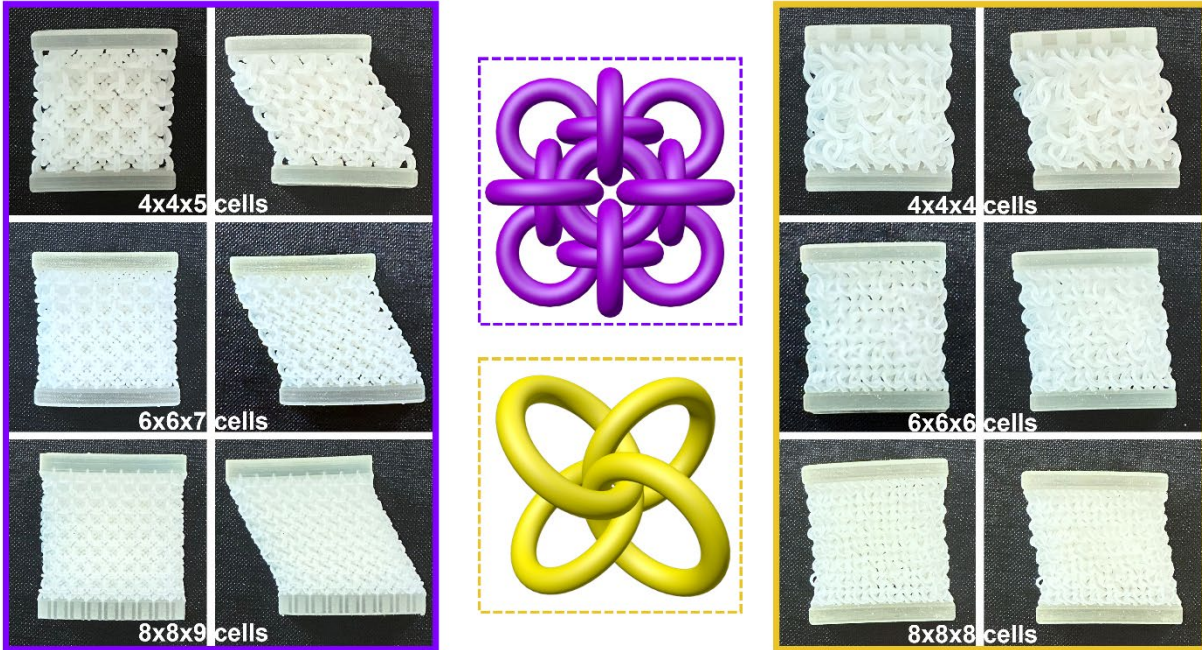
Extended Data Fig. 5. Force-displacement response of the J-2-ring PAM under uniaxial compressive loading across various initial configurations. The force responses were measured using a triaxial force sensor, which recorded forces along the loading direction (Z-axis) and two perpendicular directions (X and Y axes). The panel of images displays the different initial configurations tested, including upright, random, sheared, and twisted arrangements. The plots clearly illustrate the influence of each configuration on the global force-displacement behavior along the Z-axis. Additionally, the forces recorded in-plane (X and Y directions) display a high degree of randomness.



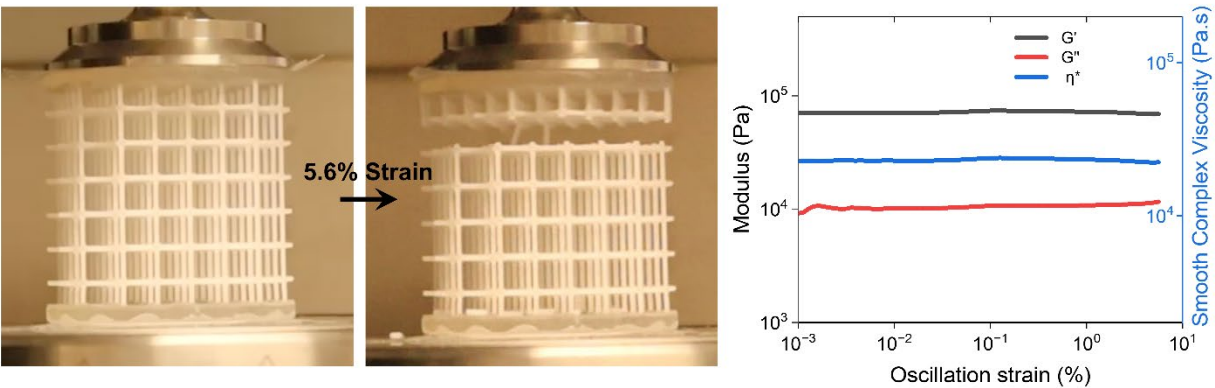
Extended Data Fig. 6. Three C-2-TT PAMs with different volume fractions. These PAM structures are fabricated at both macro- and microscale, in order to compare the scalability of PAMs' mechanical responses.



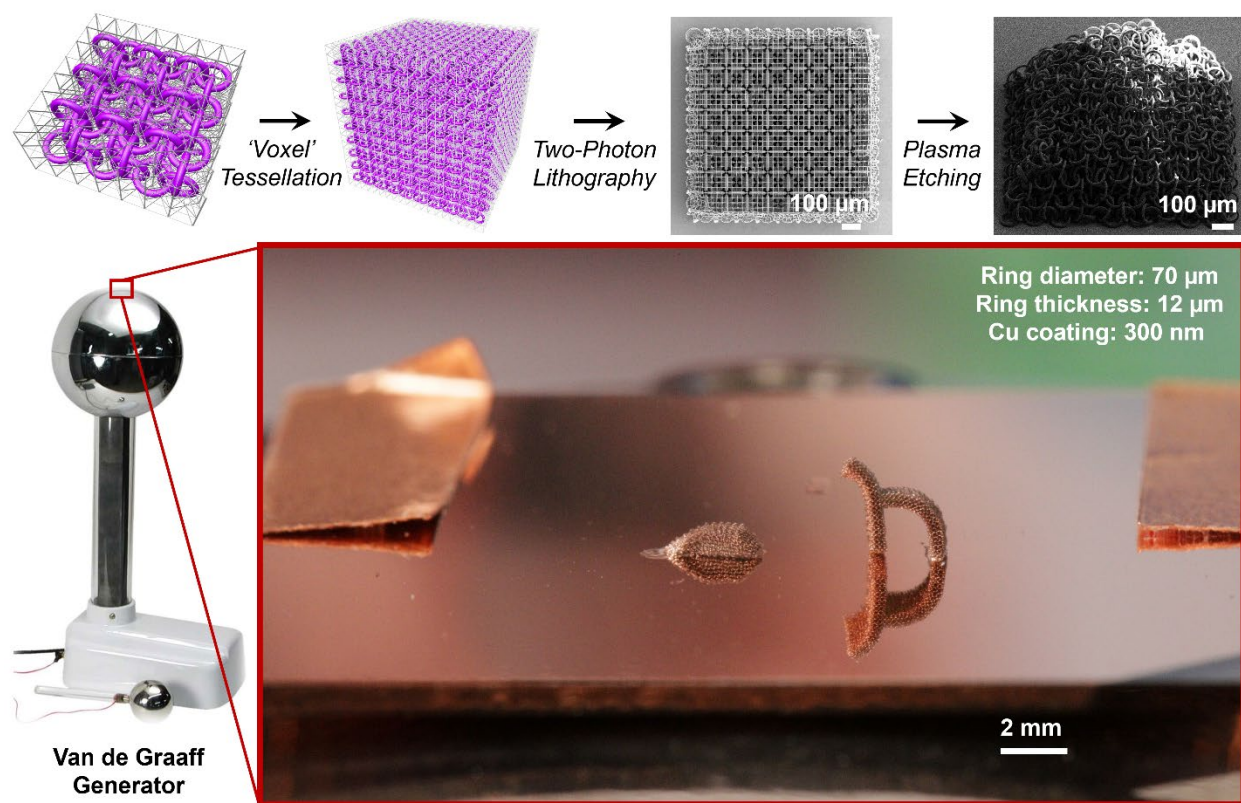
Extended Data Fig. 7. Deformability of PAM spheres with J-2-ring topology. A series of J-2-ring spherical PAMs composed of varied ring thicknesses resting on a flat surface. When oriented along the $\langle 100 \rangle$, $\langle 110 \rangle$, and $\langle 111 \rangle$ crystallographic axes, they show different adapted outline shapes, influenced by gravity. Scale bar: 2 cm.



Extended Data Fig. 8. Maximal critical shear jamming strains of J-2-ring and T-2-ring PAMs. Top-down photographs show J-2-ring (left) and T-2-ring (right) PAMs, fixed with top and bottom gripping plates, horizontally placed on a flat surface. From top row to bottom row, PAMs are designed within the same domain, but with increasing numbers of smaller unit cells. Left columns show the natural state of the PAMs, while right columns show PAMs at their critical shear jamming strains.



Extended Data Fig. 9. Rheology test of simple cubic truss lattice. Experimental setup and results of an amplitude sweep test using a simple cubic truss lattice, with consistent configurations as the tests on PAMs. The test was automatically stopped at an oscillation strain of 5.6%, due to a catastrophic failure developed across one layer in the sample.



Extended Data Fig. 10. Fabrication and electrostatic reconfiguration of μ -PAM. Top row shows the design, two-photon lithography, and plasma etching process of a J-2-ring PAM. Bottom panel illustrates Cu-plated μ -PAM samples attached to ITO-coated glass substrates, placed atop a Van de Graaff generator.

Extended Data Table 1. Designed and relaxed dimensions of PAMs.

Name	Measured width (mm)	Measured depth (mm)	Measured height (mm)	Designed edge length (mm)	Relaxed volume fraction (%)
J-2-ring	54.50	54.50	54.00	55.00	31.84
J-2-sqr*	56.25/42.78	56.25/43.79	56.25/42.27	56.50	15.67/35.23
T-2-ring	46.40	46.40	42.03	50.00	25.67
T-2-hex	47.49	47.48	46.45	50.00	22.11
J-2-oct	55.80	55.80	56.93	58.00	16.77
S-4-oct	54.20	54.20	52.40	56.00	10.87
D-3-tet	59.20	59.20	58.20	60.00	12.68
C-2-TT	47.96	47.96	47.96	49.00	32.74

*J-2-sqr has two stable configurations (see Supplementary Videos 7, 8), therefore we listed measured dimensions for configurations L/S.

Supplementary Videos:

Supplementary Video 1. Comparison between a fused and a regular J-2-ring PAM.

Supplementary Video 2. Representative compression test videos (50x speed).

Supplementary Video 3. A representative simple shear test video (20x speed).

Supplementary Video 4. Representative rheology test videos (20x speed).

Supplementary Video 5. Simulations of spherical J-2-ring PAMs deforming under gravity.

Supplementary Video 6. PAMs with S-4 topology but different particle geometries.

Supplementary Video 7. Two stable configurations of J-2-sqr.

Supplementary Video 8. Illustrated transition between two stable configurations of J-2-sqr.

Supplementary Video 9. Electrostatic reconfiguration of μ -PAMs on Van de Graaff generator (real time).